Spinning worlds

Schwarz, H.

5 Spin measurements of young sub-stellar companions: The case of HIP 78530 b

In collaboration with:
Matteo Brogi, Jayne Birkby, Ignas Snellen, Remco de Kok
In preparation

The chapter descibes the observations and analyses of the fourth and final object of a small CRIRES survey with the aim to measure the spin of young sub-stellar companions. The target, HIP 78530 b is orbiting its host star at a projected distance of ∼700 au, and has an estimated mass of 23 M_J at an age of 11 Myr, which suggests the brown dwarf is currently in its deuterium burning phase. At the wavelength of 2.3 µm we detect both carbon monoxide and water, and measure a $v \sin(i)$ of $12^{+2}_{-1.5}$ km s^{-1} from the rotational broadening of the lines. We make a first attempt to conduct comparitive planetology and study the spin parameters of the sample as a whole. Although the observed sample is small, we do see a correlation of spin velocity with age, which we interpret as due to the youngest objects still accreting angular momentum and their spin up through subsequent cooling and contraction.

5.1 Introduction

A planet spin rate is a fundamental observable affecting its climate, atmospheric dynamics, and magnetic field. In addition, it may shed light on its formation process and evolution. Our team has performed a small survey aimed to determine the rotation velocities of young substellar companions. Central to these observations is the combination of high-dispersion spectroscopy and high contrast imaging through adaptive optics techniques (Snellen et al., 2015). High dispersion spectroscopy is required to measure the rotational broadening of the lines. Adaptive optics is needed to suppress the scattered light from the host star at the position of the companion. In a pilot study (Snellen et al., 2014) we tested this technique on the directly imaged exoplanet β Pictoris b using the Cryogenic High-Resolution

Infrared Echelle Spectrograph (CRIRES; Kaeufl et al., 2004) on the Very Large Telescope (VLT). Subsequently, three more substellar companions were observed with CRIRES before it was taken off the telescope in July 2014 for a major upgrade. The upgraded instrument, CRIRES+ (Follert et al., 2014), will among other things be cross-dispersed resulting in an increase in instantaneous wavelength coverage by an order of magnitude. We observed the substellar companions GQ Lupi b, GSC 6214-210 b, and HIP 78530 b. They have estimated masses in the range 10-25 M_J, ages between 1 and 20 Myr, and projected orbital distances between 10 and 700 au.

This chapter describes the observations and analyses of the final target, HIP 78530 b. In Section 5.2 we characterise the HIP 78530 system, and in Section 5.3 we give the details of the observations. Sections 5.4 and 5.5 describe the data analyses, and the results are presented in Section 5.6. In Section 5.7 we conduct a comparative study from the survey. The conclusions are summarised in Section 5.8.

5.2 The HIP 78530 system

The HIP 78530 system (or alternatively HD 143567) is located in Upper Scorpius which is the youngest subgroup of the nearest OB association to the Earth. The primary is a bright (K = 6.9) blue B-type star on or near the main-sequence, with an estimated mass of 2.5 $M_\odot$ and an effective temperature of 10 500 K. The typical age of an Upper Scorpius member has been determined from isochrone fitting to 11 Myr (Pecaut et al., 2012), although a previous estimate from low-mass evolutionary models set the age to 5 Myr (Preibisch et al., 2002). Regardless, the intrinsic age dispersion of the subgroup is found to be small, on the order of a few million years (Preibisch and Mamajek, 2008; Pecaut et al., 2012).

The substellar companion HIP 78530 b was discovered by Lafrenière et al. (2011) as part of a direct imaging search in Upper Scorpius with the Gemini North Telescope. It is located 4.5″ to the south-east of the host star, corresponding to a projected separation of 710 au at 157 pc. The companion had in fact been detected previously by Kouwenhoven et al. (2005, 2007), yet it was not possible from their data to distinguish between a background star and a companion. Lafrenière et al. (2011) observed the object with both photometry and medium-resolution spectroscopy in the near-infrared (NIR) and made use of a 2-year baseline to confirm the companion nature. They determined the spectral type (M8) and estimated the effective temperature (2800 K) and mass (23 M_J) from comparison with synthetic spectra. However, Bailey et al. (2013) matched the 1 to 4 μm colours to a spectral type M3±2, thus questioning if the object is perhaps a background low-mass star,

rather than a brown dwarf companion. This concern was laid to rest by Lachapelle et al. (2015). They extended the available photometric data to include the Y-band and obtained medium resolution spectroscopy in the 0.9 to 1.15 µm range. This allowed them to extend the baseline of the archival data by one year, increasing the significance of the companion claim to 10σ. Moreover, the new spectra were fully consistent with the spectral type, mass and effective temperature reported by Lafrenière et al. (2011).

The mass and age of HIP 78530 b suggest that it is in a quasi-stable deuterium burning phase. Although the system is young, there is no observational evidence of circumstellar or circum-substellar disk material (Bailey et al., 2013). The combination of a B-type star and a brown dwarf companion is unusual, as is the extremely wide orbit. The existence of such a system blurs the distinction between planetary systems and stellar binaries and is a challenge to current formation theories.

Table 5.1: HIP 78530 system properties. Alternative identifier HD 143567 Ab.

Property	HIP 78530 A	HIP 78530 b
Spectral type	B9V[i]	M8 ± 1[ii]
Teff [K]	∼ 10500[iii]	2800 ± 200[ii]
Mass	∼ 2.5 $M_\odot$[iv]	23 ± 4 M_J[v]
P.A. [deg][ii]		140.3 ± 0.1
Ang. sep. ["][ii]	4.533 ± 0.006	
ΔK [mag][ii]	7.26 ± 0.04	
Distance [pc][vi]	156.7 ± 13	
v_{sys} [km/s][vii]	−9.0 ± 4.4	
Age [Myr][viii]	11 ± 2	

[i] Houk and Smith-Moore (1988)
[ii] Lafrenière et al. (2011)
[iii] From the spectral type, based on the temperature scale of Sherry et al. (2004)
[iv] From the models of D'Antona and Mazzitelli (1997)
[v] From the models of Baraffe et al. (1998, 2002); Burrows et al. (1997)
[vi] From the parallax of van Leeuwen (2007)
[vii] Gontcharov (2006)
[viii] Pecaut et al. (2012)

5.3 Observations

We observed the HIP 78530 system for two nights in 2014, on May 29 and June 20, as part of the ESO programme 293.C-5012(A). The observations were carried out with the high-dispersion spectrograph CRIRES at the VLT on Cerro Paranal in Chile. The first night, seeing was reported to be below the requirement of 1″, and as a result the target was observed again in June. Both nights we obtained a standard set of calibration frames and 18 science exposures of 120 seconds each. The target was observed in the K-band, centered on 2.3 μm with the standard wavelength settings for order 24. The CRIRES instrument has four Aladdin III InSB detectors (1024 x 512 pixels) which are separated by physical gaps corresponding to approximately 280 pixels. We excluded the first detector from the the data analysis, because there were very few CO lines within the wavelength range, and the detector suffered from a well-known non-linearity issue[1].

In order to maximise the spectral resolution, we applied the smallest choice of slit width (0.2″), and from our analysis of the stellar spectra, we find we have achieved a typical resolving power of 90 000. CRIRES is a long-slit spectrograph, and we aligned the slit with the position angle of the companion ($P.A. = 140.3°$, Lafrenière et al., 2011), thus observing the host star and the companion simultaneously. The companion is spatially resolved from the primary with an angular separation of 4.5″(Lafrenière et al., 2011), however, the K-band contrast ratio is 1.25×10^{-3}, and the high contrast requires the use of excellent adaptive optics. We made use of the Multi Application Curvature Adaptive Optics system (MACAO, Arsenault et al., 2003) which has the effect of both suppressing the star light and maximising the throughput.

For the major part, the observations were carried out under clear sky conditions, although on the second night there were thin cirrus clouds present for part of the observations. The airmasses were low (1.1 to 1.2), but the seeing varied considerably during both observing nights (see Table 5.2). The telescope was operated in a nodding mode, i.e. the pointing was changed sequentially by 10″ along the slit direction in a classical ABBA pattern between two positions, A and B, to allow accurate background subtraction. A small random jitter was added to each nod to improve flatfielding and hot pixel corrections.

Table 5.2: Details for the observing nights

	2014-05-29	2014-06-20
total time [min][i]	46	46
# of exposures[ii]	18	18
DIT [s][iii]	120	120
NDIT[iv]	1	1
airmass	1.1-1.2	1.1
sky conditions	clear	clear & thin cirrus
seeing ["][v]	0.9–2.95	0.5–2.85
FWHM star ["][vi]	0.23–0.33	0.19–0.31

[i] total observing time for the science exposures
[ii] total number of exposures
[iii] detector integration time
[iv] number of integrations per nod
[v] seeing range as reported in the observing log
[vi] range of measured full-width-half-maxima of the stellar profiles along the slit from the (AO-corrected) AB-combined frames

5.4 Data analysis

5.4.1 Basic data reduction

The two nights were treated individually, yet in the exact same way. The basic data reduction was performed with recipes from the CRIRES pipeline version 2.3.2 and processed with the EsoRex tool version 3.10.2. The pipeline performed dark-subtraction, flatfielding, and corrected for known bad pixels and non-linearity effects. Furthermore, EsoRex was used to combine the science frames in AB nodding pairs, thus performing a background subtraction. This resulted in a total of 9 two-dimensional spectra per night which were the starting point of the remaining analysis. The one-dimensional spectra of the star HIP 78530 A were also extracted with EsoRex from the two-dimensional AB-combined frames, applying the option of optimal extraction (Horne, 1986).

The two-dimensional spectra had the wavelength bins along the x-axis and the slit position along the y-axis. The frames were aligned in the spatial direction using the centroid of the stellar spectral trail as the reference. We cut out the rows further

[1] http://www.eso.org/sci/facilities/paranal/instruments/crires/doc/VLT-MAN-ESO-14500-3486_v93.pdf

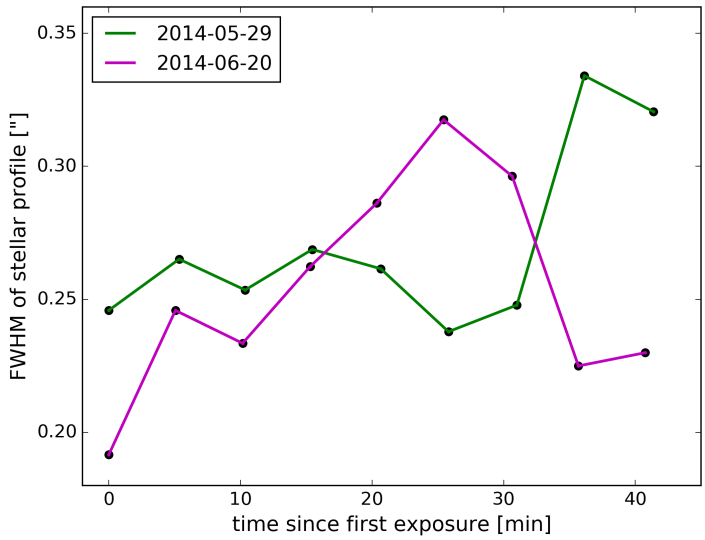

Figure 5.1: The full-width-half-maximum (FWHM) of the stellar profile along the slit direction is a proxy for the seeing, although the values will be smaller, because the two-dimensional spectra are AO-corrected. We measured the FWHM of the individual frames with a Lorentzian fit to the average stellar profile and applied this as the weights when constructing a weighted average two-dimensional spectrum for each night.

away from the stellar centroid than 100 pixels, corresponding to $\sim 8.6''$. Despite the build-in bad pixel correction of the CRIRES pipeline, the frames suffered from multiple dead pixels, hot pixels and cosmic ray hits. At distances more than $2''$ from the stellar centroid we identified bad pixels as 5σ outliers, and set their values to zero which was the mean value for pixels sufficiently far from the star to not contain scattered stellar light. The central rows $< 2''$ from the stellar centroid were not corrected for bad pixels prior to combining the frames, but instead the average frame were inspected for bad pixels.

The 9 frames were combined with a weighted average, where the weights were related to the seeing. As a seeing proxy, we made use of the full-width-half-maximum (FWHM) of the stellar point spread function. For each frame, the FWHM was determined from a Lorentzian fit to the average stellar profile along the slit direction, and it was applied as the weight of the given frame. The fitted FWHM values for both nights are shown in Fig. 5.1. It can be seen that the seeing varied considerably during both nights, but that the nights were similar on average.

The average two-dimensional spectrum was visually identified with the pro-

gramme DS9 and then corrected with cubic spline interpolation using the four nearest neighbours in the row. Strictly speaking, this was not necessary in order to extract the spectrum of the companion, but it has the advantage that the spectral trail is clearly visible in the average two-dimensional spectrum (Fig. 5.2A). To help guide the eye to the faint trail of the companion, the location is indicated with the letter 'b' on the right-hand axes.

The one-dimensional stellar spectra were treated in a similar manner. Bad pixels were visually identified and corrected with cubic spline interpolation from neighbouring pixels, and the frames were combined to a weighted average using the same weights as for the two-dimensional case.

5.4.2 Extraction of spectra for each slit position

We optimally extracted a spectrum for each slit position from the average two-dimensional spectrum (Fig. 5.2A), performing the procedure individually for the three detectors. This was done by creating a map of the stellar profiles along the slit (Fig. 5.2B) and then for each slit position we extracted a spectrum as a weighted average of the closest ± 10 slit positions with the weights determined from the profile map. The map was constructed by fitting the curvature in the stellar continuum for each of the 21 most central rows. We will refer to the extracted spectra collectively as the spatial spectra. An example from the first night, detector 4, is displayed in Fig. 5.2C. The peak intensity of the spectral trail of this detector shifts by 10 pixels in the spatial direction from one end of the detector to the other (Fig. 5.2A and 5.2B), but following the optimal extraction, the tilt is fully corrected (5.2C).

The stellar spectrum of a B-type star such as HIP 78530 A is featureless in the near infrared, but the observed stellar spectrum contains telluric lines. It is described how we extracted the one-dimensional stellar spectrum in Sec. 5.4.1, and we made use of this as a reference spectrum to remove the telluric contamination from the spatial spectra, including at the position of the companion. The reference spectrum was scaled to the flux level of the given slit position and subtracted from the spatial spectrum, followed by a normalisation. The resulting residual spatial spectra are shown in Fig. 5.2D.

The location of the companion spectrum on the detectors fall halfway between two rows of pixels, and in the following cross-correlation analysis we used the average spectrum of those two rows in the one-dimensional treatment, from which we determine the projected rotational velocity ($v \sin(i)$) of the companion. The final thermal spectrum from combining the two nights is displayed in Fig. 5.6. It is described in Sec. 5.5.2 how the weights of the two different nights were determined.

As a starting point for the wavelength solution we made use of a previous solution from the data analysis of GSC 6214-210 (Chapter 3), which was observed on

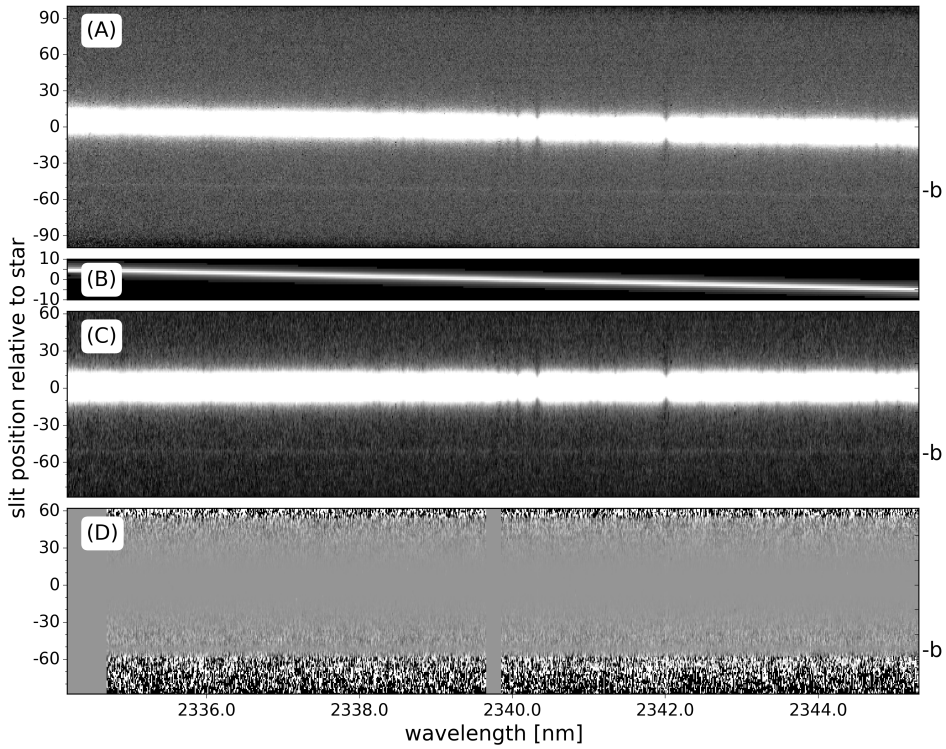

Figure 5.2: Illustration of the data analysis steps from detector 4 as observed on 2014-05-29. The *y*-axes depicts the slit position relative to the average centroid of the stellar profile. The companion position is indicated by a 'b' on the right-hand axes. The greyscales were adjusted individually for each array with an IRAF-like z-scale algorithm. *Top to bottom:* (A) The average two-dimensional spectrum, where the individual AB-combined frames were weighted by the FWHM of the stellar profile as given in Fig. 5.1. (B) A map of the stellar profiles made by fitting the continuum of each of the central rows. (C) The spatial spectra, extracted by applying the stellar profile map as weights for each slit position. Each row corresponds to an optimally extracted spectrum for the given slit position. (D) The residual spatial spectra after removing the scaled stellar spectrum, dominated by telluric lines.

the same night as one of the two nights of the HIP 78530 data set. The wavelength solution was updated for both nights through cross-correlating with a template telluric spectrum. The template spectrum was a sky transmission model from ESO SkyCalc[2] with the airmass set to 1.1 and the precipitable water vapor set to the seasonal average for the Cerro Paranal observing site.

[2]https://www.eso.org/observing/etc/skycalc

5.5 Cross-correlation analysis

The cross-correlation analysis we applied to the HIP 78530 data set followed the procedures of Chapters 2 and 3, incorporating the best elements from each of the two slightly different approaches. The concept is that although the companion spectrum is observed with a low S/N, molecules can be uniquely identified by cross-correlating with template spectra, and the rotational broadening can be measured from the shape of the cross-correlation signal. This works because the cross-correlation function (CCF) collects the signal from all of the molecular lines within the wavelength range, and because the shape of the CCF is sensitive to the average shape of the individual molecular lines. The cross-correlation signal also reveals the radial velocity (RV) of the companion.

For consistency we used the same three models which were applied in the cross-correlation analyses of GQ Lupi b (Chapter 2) and GSC 6214-210 b (Chapter 3). These are: a CO model, a H_2O model, and a model containing both CO and H_2O. Fig. 2 in Chapter 3 illustrates the three models for the same wavelength coverage which was used in this work, and the details of the models are given in Sec. 5.1. The model spectrum was convolved to the spectral resolution of CRIRES (90 000), then Doppler shifted over the range $-200\,\mathrm{km\,s^{-1}}$ to $200\,\mathrm{km\,s^{-1}}$ in steps of $1.5\,\mathrm{km\,s^{-1}}$, and cross-correlated with the residual spatial spectra. The cross-correlation was performed separately for each night and each detector.

5.5.1 Molecular detection maps

In an analogous manner to Sec. 5.2 of Chapter 2, we cross-correlated the entire array of residual spatial spectra with a model, producing what we will call a 'molecular detection map'. A row in the map corresponds to the CCF for the spectrum of a particular slit position, and the map thus provides an illustration of the strength of the cross-correlation as a function of slit position and radial velocity. If the molecule(s) in the model is present in the observed spectrum of the companion, this will give rise to an intensity peak at the known angular separation from the star and at a radial velocity which is consistent with the systemic velocity. Performing the cross-correlations for the entire array provides a means to investigate the strength of spurious signals.

5.5.2 Measuring the companion $v \sin(i)$ and RV

As described in Sec. 5.4.2, we have defined the companion spectrum as the average of the two rows of the residual spatial spectrum array which contain significant flux from the companion. We will refer to the CCF from the companion spectrum

and one of the models, as a *measured CCF*. We followed the procedures of Sec. 5.2 in Chapter 3, as well as the nomenclature for the cross-correlation functions as given in Table 2 of Chapter 3. In particular, we applied the same approach to determine the relative weights of the two nights and of the detectors. The principle is to inject the model spectrum into the companion spectrum, and then retrieving it through the cross-correlation with the same model. Subtracting the *measured CCF* from the *injected CCF* provides an estimate of the expected cross-correlation signal. The weights are then determined as the ratio of the signal estimate to the standard deviation of the *measured CCF* of the given night and detector (eq. 2, Chapter 3). The weights take several factors into account: the strength and number of lines of a given detector, and the data quality of the given night and detector. The weights were normalised and applied when combining the data or the CCFs from the two nights and the three detectors. For example when combining the molecular detection maps, the applied weights were determined from injecting the appropriate model. The weights from the CO model was applied to combine the companion spectra of the two nights into the final thermal spectrum as shown in Fig. 5.3.

The projected rotational velocity and the radial velocity of the companion were determined by fitting *model CCFs* to the signal of the *measured CCF*. The *model CCFs* were constructed by cross-correlating the model with a rotationally broadened and Doppler shifted version of itself. We tested $v \sin(i)$ values in the range $0\,\mathrm{km\,s^{-1}}$ to $60\,\mathrm{km\,s^{-1}}$ and Doppler shifts in the range $-20\,\mathrm{km\,s^{-1}}$ to $10\,\mathrm{km\,s^{-1}}$, both with step sizes of $0.5\,\mathrm{km\,s^{-1}}$. The *model CCFs* were scaled and offset (y-direction) with a least squares fit to the *measured CCF*. The best fit $v \sin(i)$ and RV values were determined with $\mathcal{X}^2$ minimisation, and the confidence intervals were determined from rescaling the errors so $\bar{\mathcal{X}}^2 = 1$. All radial velocities in the results are given in the heliocentric frame.

5.6 Results

We have measured the high-dispersion 2.3 μm thermal spectrum of the substellar companion HIP 78530 b. The spectrum is shown in Fig. 5.3. We achieved a S/N of the spectrum of 1.8 in detector 2, and 2.2 in detectors 3 and 4. In general, the individual molecular lines of the thermal spectrum are hidden within the noise, yet hints of the most prominent CO absorption lines can be seen in detectors 3 and 4. A particularly recognisable feature is the CO band-head in detector 3 at $\sim$2322.6 nm.

The presence of CO in the atmosphere of HIP 78530 b is confirmed by the cross-correlation analysis, and we also detect H_2O. Fig. 5.4 displays the molecule

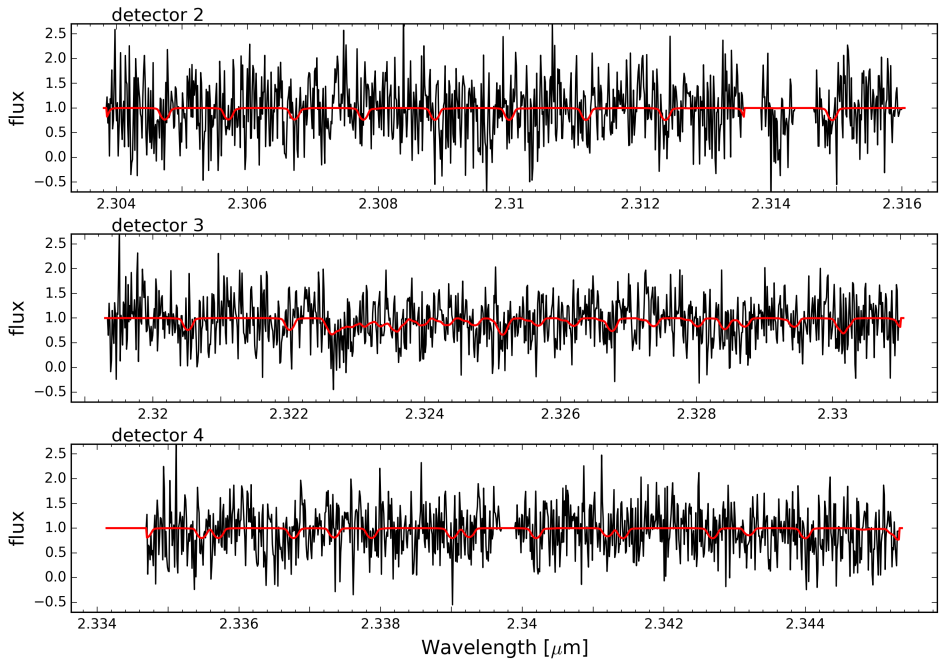

Figure 5.3: The thermal spectrum of HIP 78530 b (black). The individual observing nights were combined as a weighted average, where the weights were determined as part of the cross-correlation analysis. The red line is the CO model, convolved to the CRIRES spectral resolution, rotationally broadened to match the measured $v \sin(i)$ of 12 km s^{-1}, and Doppler shifted to match the systemic velocity of -9 km s^{-1}.

detection maps for the three models: Single-trace-gas models with CO or H_2O, and a model containing traces of both molecules. The residual spatial spectra (Fig. 5.2D) were cross-correlated with the models, so that each row of the molecule detection map is the CCF for a given position along the slit of the spectrograph. A strong signal is seen at the expected distance from the star and at a radial velocity corresponding to the systemic velocity for both the CO and CO+H_2O model. They have peak S/N values of 5.4 and 6.2, respectively. The H_2O model gives rise to a weaker signal with a peak S/N of 3.8. The water detection is seen more clearly in Fig. 5.5, which is the same as Fig. 5.4 which is a zoom-in focusing on the parameter space close to the expected position of the companion. Although the water cross-correlation signal is weak, it is located at the expected position and radial velocity.

The peak S/N values were detemined as the peak value divided through the standard deviation of the full molecular detection map in Fig. 5.4, exempting a

small region around the expected position and radial velocity. The peak S/N values underestimate the significance of the detections, because the signal is intrinsically broad, and therefore is spread over several pixels in the radial velocity direction. We used the same approach as in Chapter 3, and estimated the S/N of the molecular detections as the peak value of the CCF between the observed spectrum and the best fit rotationally broadened model, divided with the standard deviation of the difference between that same *broad measured CCF* and the auto-correlation function of the rotationally broadened model. From this we find that CO is detected with a S/N of 9.8, H_2O with one of 3.5 and the CO^+H_2O model is detected with a S/N of 9.4.

Already from Fig. 5.5 it can be seen that the cross-correlation signal is broadened, not only from CO, but also water. We measure the rotational broadening from the cross-correlation between the CO model and the extracted companion spectrum as given in Fig. 5.3. The resulting one-dimensional cross-correlation function is shown in Fig. 5.6. The $v \sin(i)$ and radial velocity is determined by fitting this *measured CCF* with *model CCFs*, minimising the $\mathcal{X}^2$, as described in Section 5.5.2. We find that the best fit *model CCF* has a $\boldsymbol{v \sin(i)}$ **of** $\mathbf{12^{+2.0}_{-1.5}\,km\,s^{-1}}$ and an **RV of** $\mathbf{-9.5 \pm 1.0\,km\,s^{-1}}$. The $v \sin(i)$ measurement is intermediate compared to the few existing measurements for other sub-stellar companions. The comparison is further discussed in Sec. 5.7. The measured radial velocity is fully consistent with the systemic velocity ($9\,km\,s^{-1}$), as expected for a companion orbiting $\sim$710 au from the central star. The expected circular orbital velocity at the observed orbital distance of HIP 78530 b is $1.8\,km\,s^{-1}$.

The orientation of the spin axis of HIP 78530 b is unknown, and therefore the measured projected rotational velocity can only be considered a lower limit on the equatorial rotation velocity. Assuming the object is viewed edge-on, the measured spin velocity corresponds to a rotational period of 26 hours, where we have applied an estimated radius of 2.5 R_J. The radius estimate is based on the effective temperature and luminosity as measured by Lachapelle et al. (2015), and checked against brown dwarfs cooling models by Burrows et al. (2001). The radius should be quasi-stationary for a few million years, yet eventually the intensity of the deuterium burning will diminish, and the radius will contract towards 1 R_J, causing the brown dwarf to spin-up to a rotational velocity of $30 \pm 7\,km\,s^{-1}$.

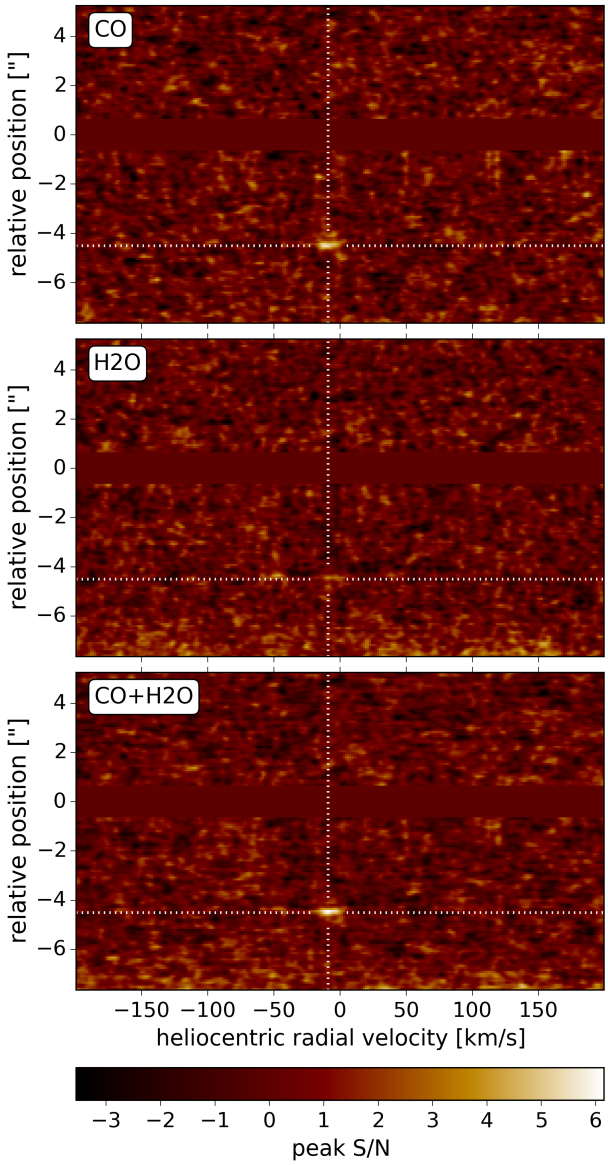

Figure 5.4: Molecule detection maps for the CO, H_2O and CO+H_2O models. The colour scale indicates the strength of the cross-correlation as a function of radial velocity and slit position relative to the host star. The expected position of the planet is indicated by the white dotted lines, corresponding to the systemic velocity and the known angular separation of the companion. The companion is detected for all three models. See also Fig. 5.5 for the enlarged images centered on the companion signals.

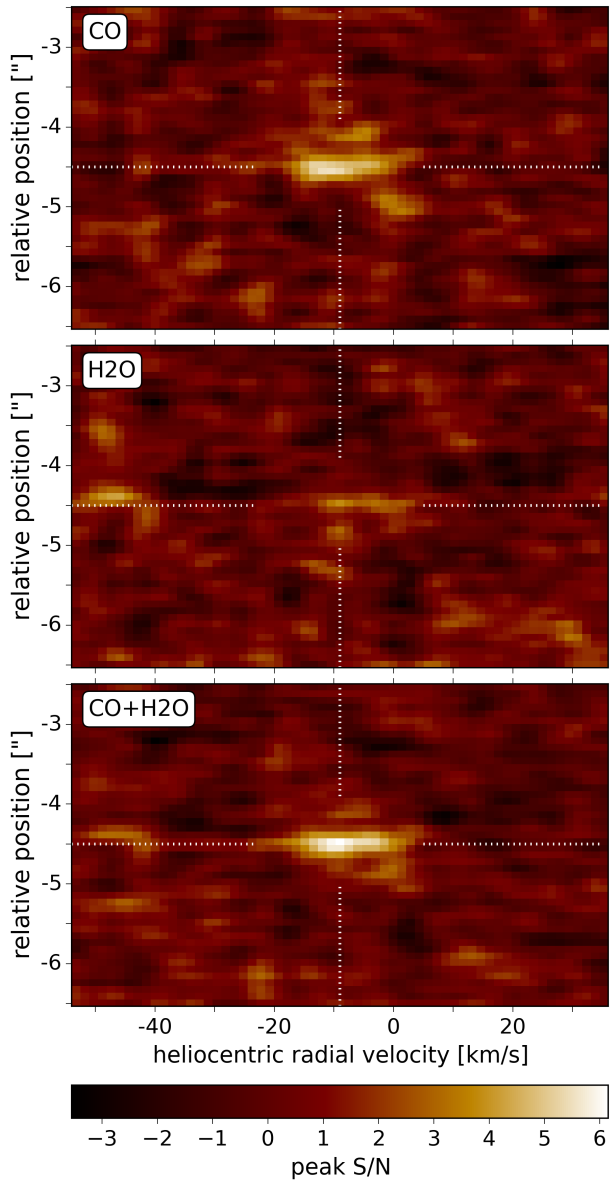

Figure 5.5: Same as Fig. 5.4, but centered around the planet signals and enlarged to show the details. The peak S/N values are 5.4 for CO, 3.8 for H_2O, and 6.2 for the CO+H_2O model. The peak S/N values underestimate the significance of the molecular detections, since this is the cross-correlation with the unbroadened models.

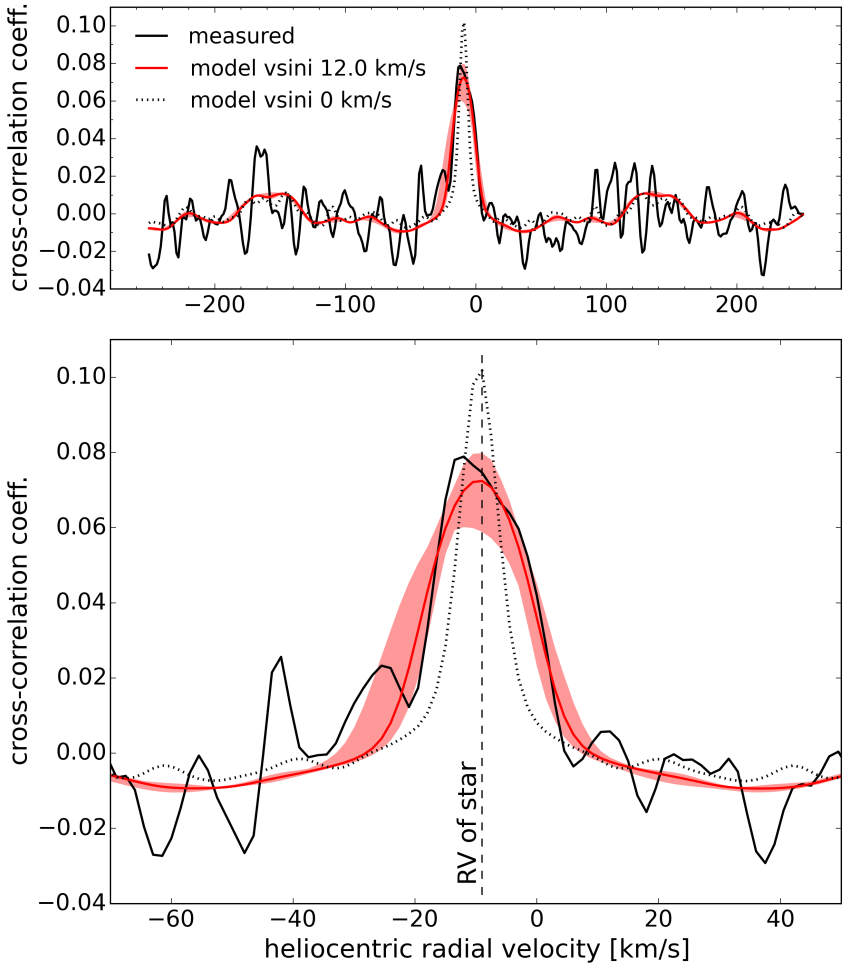

Figure 5.6: The measured cross-correlation function (CCF) from the unbroadened CO model and the observed companion spectrum (solid black line). The CO signal is centered roughly on the radial velocity of the host star ($-9\,\mathrm{km\,s^{-1}}$), and the best fit model CCF (solid red line) has a rotational broadening of $12\,\mathrm{km\,s^{-1}}$. The red shading indicates the 2σ confidence. The auto-correlation function of the unbroadened model is plotted for comparison as the dotted black line. The lower panel is an enlarged version of the central radial velocities of the upper panel.

5.7 Towards a comparative study of exoplanet spin

Only a handful of substellar companions have a measurement of their spin: Two exoplanets, and including this work, three low-mass brown dwarfs. The five objects are listed in Table 5.7 with a collection of properties which are relevant to a comparative study of their spin. Four of these objects were observed as part of the same CRIRES survey that this work is based upon. These are β Pictoris b which has a $v \sin(i)$ of 25 km s^{-1}, GSC 6214-210 b with $v \sin(i) = 21.5$ km s^{-1}, HIP 78530 b with $v \sin(i) = 12$ km s^{-1}, and GQ Lupi b with $v \sin(i) = 5.3$ km s^{-1}. The fifth object is 2M1207 b, for which Zhou et al. (2016) measured the rotation period to be 10.7 hours from the rotational modulations in the combined lightcurve of the host star and the companion. This corresponds to an equatorial rotation velocity (v_{eq}) of 17.3 km s^{-1} when applying a radius estimate based on the planet cooling models from Burrows et al. (2001). It is important to realise that the $v \sin(i)$ measurements are lower limits of the equatorial rotation velocities, and that the inclinations are unknown, meaning that for the individual object v_{eq} could be significantly larger than the measured $v \sin(i)$. It is still meaningfull to compare the measured spins to one another, keeping in mind that the small sample size comes with some limitations.

The five objects show a wide range of spin velocities ($v \sin(i)$ or v_{eq}), ranging from 5 km s^{-1} to 25 km s^{-1}. We have investigated the correlation of the spin velocities with their masses, ages and orbital semi-major axes, as well as the correlation of the specific angular momentum with the same three properties. The results are shown in the six panels of Fig. 5.7. The specific angular momentum is calculated based on the $v \sin(i)$ measurement and the estimated radii. We note that the unknown inclinations are not included in the errorbars of the specific angular momenta, which are instead dominated by the uncertainties in the radii.

The first row of Fig. 5.7 shows the spin velocity and the specific angular momentum, both as a function of mass. There is no clear trend with mass, based on these five objects. This stands in contrast to the solar system planets which have a clear trend: The more massive planets spin faster (Hughes, 2003). The spin velocities of the substellar companions are plotted together with the solar system planets in Fig. 5.8. From this we see that β Pictoris b and 2M1207 b, and possibly also GSC 6214-210 b, are roughly consitent with the Solar System trend, although they fall slightly below an extrapolation of the solar system planets. This can be explained by the young ages of the objects, as they are expected to spin up as they cool and contract, which will result in spin velocities in better agreement with the observed solar system correlation.

It is interesting that the three objects which are best matched to the Solar

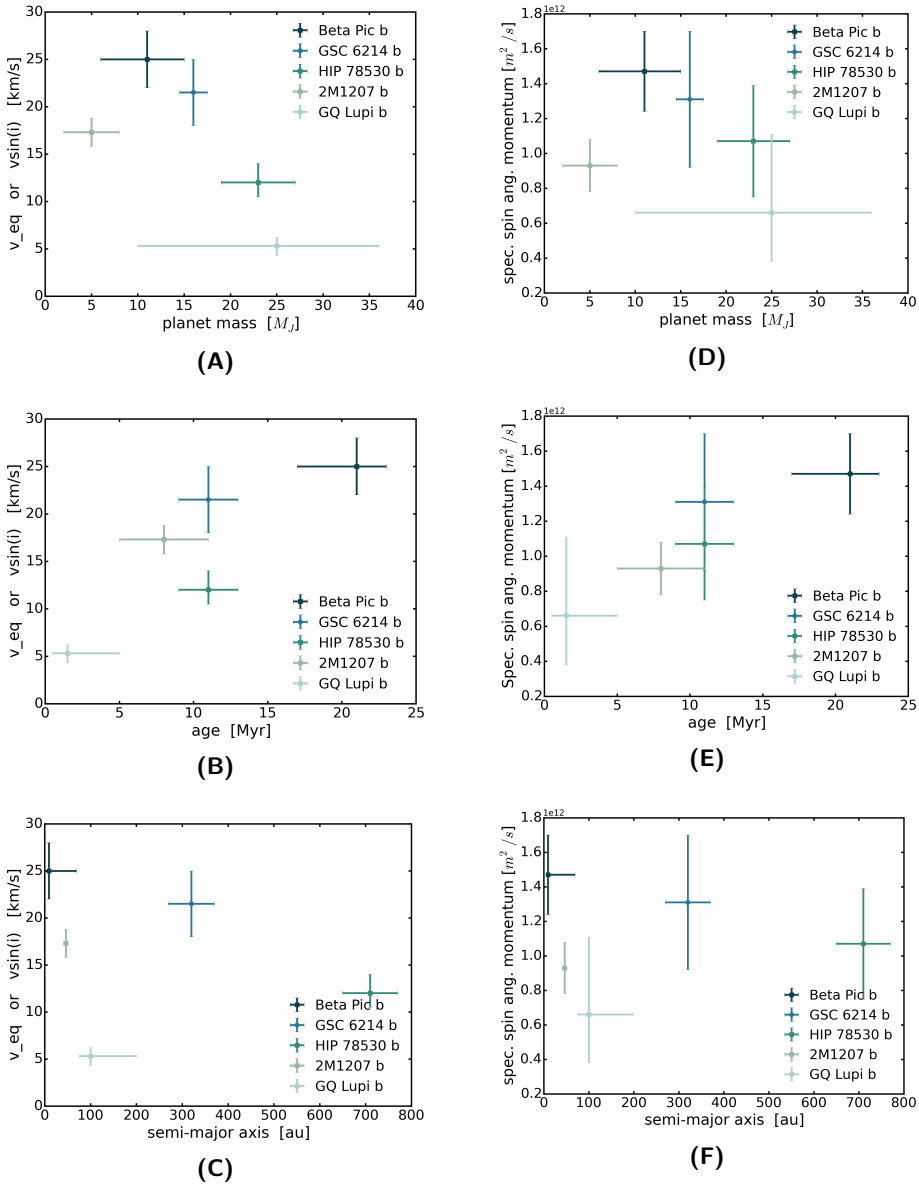

Figure 5.7: Comparison of substellar companions with a spin measurement. The left column shows the projected rotational velocity as a function of mass, age and semi-major axis, except in the case of 2M1207 b which has an equatorial rotation velocity derived from the rotation period. The right column is the same for the specific angular momentum derived from the spin velocity and the estimated radii of the objects.

Table 5.3: Properties of substellar companions with spin measurements.

	β Pictoris b	2M1207 b	GQ Lupi b	GSC 6214 b	HIP 78530 b
spectral type	L1 $\pm$ 1.5[i]	L5[ii]	L1.5[ii]	M9 $\pm$ 0.5[iii]	M8 $\pm$ 1[iv]
mass [M_J]	11 $\pm$ 5[v]	5 $\pm$ 3[vi]	25^{+11}_{-15}[vii]	16 $\pm$ 1.5[iii]	23 $\pm$ 4[iv]
Teff [K]	1600^{+50}_{-25}[viii]	1230 $\pm$ 310[ix]	2650 $\pm$ 100[x]	2300 $\pm$ 200[iii]	2800 $\pm$ 200[iv]
radius [R_J]	1.65 $\pm$ 0.06[viii]	1.5 $\pm$ 0.1[xviii]	3.5 $\pm$ 1.5[x]	1.7 $\pm$ 0.2[xviii]	2.5 $\pm$ 0.3[xviii]
semi-major axis [au]	9^{+4}_{-3}[xi]	46 $\pm$ 5[ix]	100^{+100}_{-25}[xii]	320 $\pm$ 50[iii]	710 $\pm$ 60[iv]
age [Myr]	21 $\pm$ 4[xiii]	8 $\pm$ 3[ix]	$1.5^{+3.5}_{-1}$[xii]	11 $\pm$ 2[xiv]	11 $\pm$ 2[xiv]
$v \sin(i)$ [km s^{-1}]	25 $\pm$ 3[v]	-	$5.3^{+0.9}_{1}$[xii]	21.5 $\pm$ 3.5[xvi]	$12^{+2}_{-1.5}$[xvii]
v_{eq} [km s^{-1}]	-	17.3 $\pm$ 1.5[xv]	-	-	-

[i] Bonnefoy et al. (2014) [ii] Faherty et al. (2009) [iii] Lachapelle et al. (2015)
[iv] Lafrenière et al. (2011) [v] Snellen et al. (2014) [vi] Ducourant et al. (2008)
[vii] Ginski et al. (2014) [viii] Currie et al. (2013) [ix] Song et al. (2006) [x] Seifahrt et al. (2007)
[xi] Lecavelier des Etangs and Vidal-Madjar (2016) [xii] Schwarz et al. (2016) [xiii] Binks and Jeffries (2014)
[xiv] Pecaut et al. (2012) [xv] Zhou et al. (2016) [xvi] Schwarz et al. in prep [xvii] This work
[xviii] From planet / brown dwarf cooling models (Burrows et al., 2001), and / or luminosity and temperature.

System trend are also the ones with the lowest masses. However, the spin-evolution of planets and brown dwarfs is expected to be a complicated function of both age and mass, and in particular very young objects (age $\leqslant$ 100 Myr), such as the ones in this sample. Their spin will be very sensitive to their age, due to the mass-dependent evolution of the radius as the objects cool and contract. The sensitivity to age is evident from Figures 5.7C and 5.7D: Both the spin velocity and the specific spin angular momentum correlates with age.

It is possible we are also seeing an effect with mass. GSC 6214-210 b and HIP 78530 b are both located in Upper Scorpius, which is reported to have a small instrinsic age dispersion (Preibisch and Mamajek, 2008; Pecaut et al., 2012). Therefore the two substellar companions are likely to have approximately the same age, yet they spin with different rotational velocities. Assuming that this is not a simple effect of the viewing geometry, we can speculate that HIP 78530 b rotates more slowly because it is the more massive of the two. With a mass of 23 M_J and an age of 11 Myr, HIP 78530 b is expected to be in a deuterium burning phase, which inflates the radius, temporarily preventing the brown dwarf from contracting and spinning up. We may thus be seeing the beginnings of mass-dependent evolutionary tracks. Assuming no external influences, the spin angular momentum evolution of giant planets can be divided into three phases: The first one is dominated by accretion, and this is followed by a period dominated by contraction and a rapid spin-up, and finally a quasi-stable phase when the contraction has slowed down significantly.

In the case of brown dwarfs, the situation is a little more complicated. As mentioned above the more massive brown dwarfs ($<$ 18 M_J) will be influenced significantly by deuterium burning, which will temporarily slow the contraction. Following this deuterium burning stage the brown dwarf will rapidly contract (Burrows et al., 2001). In the final phase, the more massive brown dwarfs may also be affected by magnetic braking from winds (Reiners and Basri, 2008), so if the Solar System trend holds for old wide-orbit exoplanets and brown dwarfs, the spin versus mass relation could have a turn-off point. In Chapter 3, we speculated that GQ Lupi b is in the phase dominated by accretion, and it may therefore yet gain a significant amount of spin angular momentum. This is supported by observational evidence of ungoing accretion (Seifahrt et al., 2007; Zhou et al., 2014). GSC 6214-210 b, HIP 78530 b and possibly also 2M1207 b are more likely to be in the contraction phase. There is observational evidence for ongoing accretion on GSC 6214-210 b, but ALMA observations constrained the mass accretion rate and found it to be unlikely that the object will still gain a significant amount of mass. β Pictoris b is the oldest, and with a mass of only 11 M_J, the contraction will already have slowed significantly, although it will remain in the contraction phase for another

~ 100 Myr.

In the end it is expected that all these sub-stellar objects will contract to a radius within 30% of that of Jupiter. Speculating, in the future, when we have gained enough knowledge about the spin evolution of sub-stellar companions, it may be possible to invert the problem and determine the ages of companions through their spin state - although this does require knowledge of the viewing angle of the planet, which could be obtained by combining $v \sin(i)$ measurements with photometric monitoring to determine the rotation period. If this could be done with sufficient accuracy, one can identify the precise stage of the early star formation process during which the planet is formed.

The two bottom panels of Fig. 5.7 show the $v \sin(i)$ as function of orbital semi-major axis. Although no trends are seen for these five planets, such diagrams can in the future maybe be used to differentiate between different formation processes. E.g. those substellar companions seen at the largest orbital distances are more likely to have formed through gravitational instability, while those at shorter distances through core accretion. This may, if sufficient objects are observed, show up as a bi-modal distribution in planet spin and/or specific spin angular momentum.

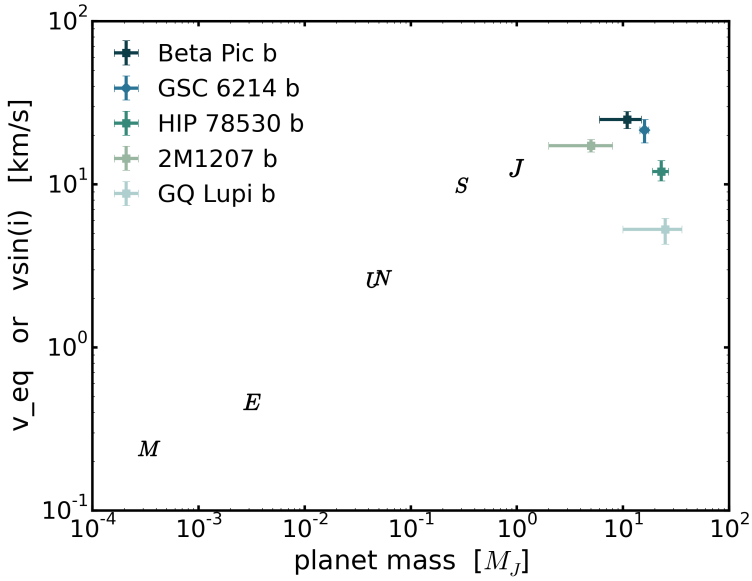

Figure 5.8: The equatorial rotation velocity (2M1207 b) or the projected rotational velocity (the remaining 4) for the sub-stellar companions which have a measurement of one of these quantities. For comparison, the equatorial rotation velocities of the solar system planets are also shown, with the exception of Mercury and Venus which have spins dominated by tidal interactions with the Sun.

5.8 Conclusions

In this chapter we described the CRIRES observations and analysis of the substellar companion, HIP 78530 b, which show a projected spin velocity of $12^{+2.0}_{-1.5}$ km s^{-1} from the rotational broadening of its carbon monoxide lines. This is well within the range of the observed $v \sin(i)$ values of the other objects in the sample. Although the observed sample is small, these are the first substellar companions for wich the $v \sin(i)$ is measured (in addition to $P_{\rm rot}$ for 2M1207 b; Zhou et al., 2016). We see a correlation of spin velocity with age, which we interpret as due to the youngest objects still accreting angular momentum and their spin up through subsequent cooling and contraction. We also note that HIP 78530 b rotates slower than GSC 6214-210 which is expected to have the same age since they are both located in the Upper Scorpius group. Although this could simply be a projection effect, it could also be related to the higher mass of HIP 78530 b, implying it is currently in its deuterium burning phase - slowing its cooling and contraction and subsequent spin-up. The major upgrade of the CRIRES instrument (CRIRES+; Follert et al., 2014), which will come online in 2018, with an increase in instantaneous wavelength coverage of an order of magnitude, will mean that in principle the $v \sin(i)$ of *all* directly imaged exoplanets can be measured. This will be fundamental in disentangling mass, age, and possibly orbital separation effects linked to formation and evolutionary processes.

References

Arsenault, R., J. Alonso, H. Bonnet, J. Brynnel, B. Delabre, R. Donaldson, C. Dupuy, E. Fedrigo, J. Farinato, N. N. Hubin, L. Ivanescu, M. E. Kasper, J. Paufique, S. Rossi, S. Tordo, S. Stroebele, J.-L. Lizon, P. Gigan, F. Delplancke, A. Silber, M. Quattri, and R. Reiss
2003. MACAO-VLTI: An Adaptive Optics system for the ESO VLT interferometer. In *Adaptive Optical System Technologies II*, P. L. Wizinowich and D. Bonaccini, eds., volume 4839 of *Society of Photo-Optical Instrumentation Engineers (SPIE) Conference Series*, Pp. 174–185.

Bailey, V., P. M. Hinz, T. Currie, K. Y. L. Su, S. Esposito, J. M. Hill, W. F. Hoffmann, T. Jones, J. Kim, J. Leisenring, M. Meyer, R. Murray-Clay, M. J. Nelson, E. Pinna, A. Puglisi, G. Rieke, T. Rodigas, A. Skemer, M. F. Skrutskie, V. Vaitheeswaran, and J. C. Wilson
2013. A Thermal Infrared Imaging Study of Very Low Mass, Wide-separation Brown Dwarf Companions to Upper Scorpius Stars: Constraining Circumstellar Environments. *ApJ*, 767:31.

Baraffe, I., G. Chabrier, F. Allard, and P. H. Hauschildt
1998. Evolutionary models for solar metallicity low-mass stars: mass-magnitude relationships and color-magnitude diagrams. *A&A*, 337:403–412.

Baraffe, I., G. Chabrier, F. Allard, and P. H. Hauschildt
2002. Evolutionary models for low-mass stars and brown dwarfs: Uncertainties and limits at very young ages. *A&A*, 382:563–572.

Binks, A. S. and R. D. Jeffries
2014. A lithium depletion boundary age of 21 Myr for the Beta Pictoris moving group. *MNRAS*, 438:L11–L15.

Bonnefoy, M., G.-D. Marleau, R. Galicher, H. Beust, A.-M. Lagrange, J.-L. Baudino, G. Chauvin, S. Borgniet, N. Meunier, J. Rameau, A. Boccaletti, A. Cumming, C. Helling, D. Homeier, F. Allard, and P. Delorme
2014. Physical and orbital properties of β Pictoris b. *A&A*, 567:L9.

Burrows, A., W. B. Hubbard, J. I. Lunine, and J. Liebert
2001. The theory of brown dwarfs and extrasolar giant planets. *Reviews of Modern Physics*, 73:719–765.

Burrows, A., M. Marley, W. B. Hubbard, J. I. Lunine, T. Guillot, D. Saumon, R. Freedman, D. Sudarsky, and C. Sharp
1997. A Nongray Theory of Extrasolar Giant Planets and Brown Dwarfs. *ApJ*, 491:856–875.

Currie, T., A. Burrows, N. Madhusudhan, M. Fukagawa, J. H. Girard, R. Dawson, R. Murray-Clay, S. Kenyon, M. Kuchner, S. Matsumura, R. Jayawardhana, J. Chambers, and B. Bromley
2013. A Combined Very Large Telescope and Gemini Study of the Atmosphere of the Directly Imaged Planet, β Pictoris b. *ApJ*, 776:15.

D'Antona, F. and I. Mazzitelli
1997. Evolution of low mass stars. *Mem. Soc. Astron. Italiana*, 68:807.

Ducourant, C., R. Teixeira, G. Chauvin, G. Daigne, J.-F. Le Campion, I. Song, and B. Zuckerman
2008. An accurate distance to 2M1207Ab. *A&A*, 477:L1–L4.

Faherty, J. K., A. J. Burgasser, K. L. Cruz, M. M. Shara, F. M. Walter, and C. R. Gelino
2009. The Brown Dwarf Kinematics Project I. Proper Motions and Tangential Velocities for a Large Sample of Late-Type M, L, and T Dwarfs. *AJ*, 137:1–18.

Follert, R., R. J. Dorn, E. Oliva, J. L. Lizon, A. Hatzes, N. Piskunov, A. Reiners, U. Seemann, E. Stempels, U. Heiter, T. Marquart, M. Lockhart, G. Anglada-Escude, T. Löwinger, D. Baade, J. Grunhut, P. Bristow, B. Klein, Y. Jung, D. J. Ives, F. Kerber, E. Pozna, J. Paufique, H. U. Kaeufl, L. Origlia, E. Valenti, D. Gojak, M. Hilker, L. Pasquini, A. Smette, and J. Smoker
2014. CRIRES+: a cross-dispersed high-resolution infrared spectrograph for the ESO VLT. In *Ground-based and Airborne Instrumentation for Astronomy V*, volume 9147 of *Proc. SPIE*, P. 914719.

Ginski, C., T. O. B. Schmidt, M. Mugrauer, R. Neuhäuser, N. Vogt, R. Errmann, and A. Berndt
2014. Astrometric follow-up observations of directly imaged sub-stellar companions to young stars and brown dwarfs. *MNRAS*, 444:2280–2302.

Gontcharov, G. A.
2006. Pulkovo Compilation of Radial Velocities for 35 495 Hipparcos stars in a common system. *Astronomy Letters*, 32:759–771.

Horne, K.
1986. An optimal extraction algorithm for CCD spectroscopy. *PASP*, 98:609–617.

Houk, N. and M. Smith-Moore
1988. *Michigan Catalogue of Two-dimensional Spectral Types for the HD Stars. Volume 4, Declinations -26.0 to -12.0.*

Hughes, D. W.
2003. Planetary spin. *Planet. Space Sci.*, 51:517–523.

Kaeufl, H.-U., P. Ballester, P. Biereichel, B. Delabre, R. Donaldson, R. Dorn, E. Fedrigo, G. Finger, G. Fischer, F. Franza, D. Gojak, G. Huster, Y. Jung, J.-L. Lizon, L. Mehrgan, M. Meyer, A. Moorwood, J.-F. Pirard, J. Paufique, E. Pozna, R. Siebenmorgen, A. Silber, J. Stegmeier, and S. Wegerer
2004. CRIRES: a high-resolution infrared spectrograph for ESO's VLT. In *Ground-based Instrumentation for Astronomy*, A. F. M. Moorwood and M. Iye, eds., volume 5492 of *Society of Photo-Optical Instrumentation Engineers (SPIE) Conference Series*, Pp. 1218–1227.

Kouwenhoven, M. B. N., A. G. A. Brown, S. F. Portegies Zwart, and L. Kaper
2007. The primordial binary population. II.. Recovering the binary population for intermediate mass stars in Scorpius OB2. *A&A*, 474:77–104.

Kouwenhoven, M. B. N., A. G. A. Brown, H. Zinnecker, L. Kaper, and S. F. Portegies Zwart
2005. The primordial binary population. I. A near-infrared adaptive optics search for close visual companions to A star members of Scorpius OB2. *A&A*, 430:137–154.

Lachapelle, F.-R., D. Lafrenière, J. Gagné, R. Jayawardhana, M. Janson, C. Helling, and S. Witte
2015. Characterization of Low-mass, Wide-separation Substellar Companions to Stars in Upper Scorpius: Near-infrared Photometry and Spectroscopy. *ApJ*, 802:61.

Lafrenière, D., R. Jayawardhana, M. Janson, C. Helling, S. Witte, and P. Hauschildt
2011. Discovery of an ~ 23 M_{Jup} Brown Dwarf Orbiting ~ 700 AU from the Massive Star HIP 78530 in Upper Scorpius. *ApJ*, 730:42.

Lecavelier des Etangs, A. and A. Vidal-Madjar
2016. The orbit of beta Pictoris b as a transiting planet. *A&A*, 588:A60.

Pecaut, M. J., E. E. Mamajek, and E. J. Bubar
2012. A Revised Age for Upper Scorpius and the Star Formation History among the F-type Members of the Scorpius-Centaurus OB Association. *ApJ*, 746:154.

Preibisch, T., A. G. A. Brown, T. Bridges, E. Guenther, and H. Zinnecker
2002. Exploring the Full Stellar Population of the Upper Scorpius OB Association. *AJ*, 124:404–416.

Preibisch, T. and E. Mamajek
2008. *The Nearest OB Association: Scorpius-Centaurus (Sco OB2)*, P. 235.

Reiners, A. and G. Basri
2008. Chromospheric Activity, Rotation, and Rotational Braking in M and L Dwarfs. *ApJ*, 684:1390–1403.

Schwarz, H., C. Ginski, R. J. de Kok, I. A. G. Snellen, M. Brogi, and J. L. Birkby
2016. The slow spin of the young substellar companion GQ Lupi b and its orbital configuration. *A&A*, 593:A74.

Seifahrt, A., R. Neuhäuser, and P. H. Hauschildt
2007. Near-infrared integral-field spectroscopy of the companion to GQ Lupi. *A&A*, 463:309–313.

Sherry, W. H., F. M. Walter, and S. J. Wolk
2004. Photometric Identification of the Low-Mass Population of Orion OB1b. I. The σ Orionis Cluster. *AJ*, 128:2316–2330.

Snellen, I., R. de Kok, J. L. Birkby, B. Brandl, M. Brogi, C. Keller, M. Kenworthy, H. Schwarz, and R. Stuik
2015. Combining high-dispersion spectroscopy with high contrast imaging: Probing rocky planets around our nearest neighbors. *A&A*, 576:A59.

Snellen, I. A. G., B. R. Brandl, R. J. de Kok, M. Brogi, J. Birkby, and H. Schwarz
2014. Fast spin of the young extrasolar planet β Pictoris b. *Nature*, 509:63–65.

Song, I., G. Schneider, B. Zuckerman, J. Farihi, E. E. Becklin, M. S. Bessell, P. Lowrance, and B. A. Macintosh
2006. HST NICMOS Imaging of the Planetary-mass Companion to the Young Brown Dwarf 2MASSW J1207334-393254. *ApJ*, 652:724–729.

van Leeuwen, F.
2007. Validation of the new Hipparcos reduction. *A&A*, 474:653–664.

Zhou, Y., D. Apai, G. H. Schneider, M. S. Marley, and A. P. Showman
2016. Discovery of Rotational Modulations in the Planetary-mass Companion 2M1207b: Intermediate Rotation Period and Heterogeneous Clouds in a Low Gravity Atmosphere. *ApJ*, 818:176.

Zhou, Y., G. J. Herczeg, A. L. Kraus, S. Metchev, and K. L. Cruz
2014. Accretion onto Planetary Mass Companions of Low-mass Young Stars. *ApJ*, 783:L17.